In vivo imaging nickel-rich laticifers: a breakthrough in metal hyperaccumulation

Antony van der Ent, Kathryn Spiers, Tanguy Jaffré, Dennis Brueckner, Sarah Irvine, Peter Erskine, Vidiro Gei, Emmanuelle Montargès-Pelletier, Bruno Fogliani, Guillaume Echevarria, et al.

In vivo imaging nickel-rich laticifers: a breakthrough in metal hyperaccumulation

Antony van der Ent[1,2,3], Kathryn M. Spiers[4], Tanguy Jaffré[5,6], Dennis Brueckner[4], Sarah C. Irvine[7], Jan Garrevoet[4], Peter D. Erskine[3], Vidiro Gei[3], Emmanuelle Montargès-Pelletier[8], Bruno Fogliani[9],*
Guillaume Echevarria[2], Sandrine Isnard[5,6]

[1]Laboratory of Genetics, Wageningen University and Research, The Netherlands.

[2]Université de Lorraine, INRAE, LSE, F-54000, Nancy, France.

[3]Centre for Mined Land Rehabilitation, Sustainable Minerals Institute, The University of Queensland, Australia.

[4]Deutsches Elektronen-Synchrotron DESY, Germany.

[5]AMAP, Université Montpellier, IRD, CIRAD, CNRS, INRAE, Montpellier, France.

[6]AMAP, IRD, Herbier de Nouvelle-Calédonie, Nouméa, New Caledonia.

[7] Institute of Materials Physics, Helmholtz-Zentrum Hereon, Germany.

[8] Université de Lorraine, CNRS, LIEC, F-54000, Nancy, France.

[9]Institut Agronomique néo-Calédonien (IAC), Equipe ARBOREAL (AgricultuRe BiOdiveRsité Et vAlorisation), New Caledonia.

*Corresponding author: antony.vanderent@wur.nl

Abstract

The discovery of the nickel-rich latex of the New Caledonian endemic tree *Pycnandra acuminata* introduced the term 'hyperaccumulator' and gave rise to a new field of research. This then instigated a global quest for these unusual hyperaccumulator plants, even while the underlying mechanisms of nickel acquisition, transport, and internal elemental distribution remained unknown for this original laticifer-bearing hyperaccumulator plant. Here we reveal for the first time the distribution of nickel-filled laticifers in the different plant organs of *P. acuminata*. The pressurised nickel laticifers were imaged multimodally with a combination of synchrotron X-ray fluorescence (XRF) microscopy, microtomography (XRF-μCT) and synchrotron X-ray phase contrast imaging microtomography (PCI-μCT). These advanced synchrotron methodologies allowed for complimentary non-invasive reconstructions of an *in-situ* model of the laticiferous system in this species. The data shows the distribution of the nickel-rich laticifers within whole plant tissues from roots to apical tip, thus suggesting nickel trafficking in the laticifer network. The extraordinary concentration of nickel within *P. acuminata* laticifers functions as an effective natural tracer for XRF-μCT and PCI-μCT to probe the structure and organization of these cells, thereby permitting insights into the development and physiological functioning of this unique duct system.

Keywords: fluorescence tomography; hyperaccumulation; laticifers transport; nickel trafficking; PCI-μCT; *Pycnandra acuminata*; XRF-μCT; X-ray fluorescence (XRF).

Introduction

The discovery of vivid blue-green latex (Fig. 1a) that contained 25 Wt% nickel (Ni) in the New Caledonian endemic tree *Pycnandra acuminata* (Baill.) Swenson & Munzinger (Sapotaceae) led to the term 'hyperaccumulator' (Jaffré et al., 1976) and gave rise to a new field of research (Jaffré et al., 2018). While the extreme behaviour exhibited by hyperaccumulator plants that results from specific metal(loid) uptake, transport and sequestering mechanisms have been widely studied (Rascio & Navari-Izzo, 2011; Leitenmaier & Küpper, 2013; Andresen et al., 2018), the unusual Ni-rich laticifers found in *P. acuminata* remain overlooked. In most Ni hyperaccumulator plants, the preferential storage location is in the foliar epidermal cells, and specifically in the vacuoles where the Ni^{2+} does not interfere with photosynthesis and respiration (Küpper et al., 2001). In *P. acuminata*, although Ni has also been found in vacuoles of leaf epidermal cells (Perrier et al., 2004; Gei et al., 2020), the extraordinarily high Ni concentration in laticifers suggests that they are a key storage site for Ni hyperaccumulation (Jaffré et al., 1976; Sagner et al., 1998; Isnard et al., 2020).

Laticifers are specialised cells with a tuberous shape that secrete and accumulate latex (Metcalfe, 1967; Mahlberg, 1993; Hagel et al., 2008; Johnson et al. 2021). Latex is produced by laticifers in response to physical damage and has important functions against herbivory or infection (Farrel, 1991; Ramos et al. 2019; Freitas et al., 2024). In the cytoplasm of laticifers, latex is phytochemically diverse and often contains complex mixtures of terpenoids, phenolics, proteins, and alkaloids (Agrawal & Konno, 2009). Their widespread occurrence in the plant kingdom (laticifers are present in ~10% of all angiosperms globally) and their chemical diversity have attracted attention over the last twenty years (Castelblanque et al., 2016; Nawrot, 2020; Johnson et al. 2021; Freitas et al., 2024). Recent studies have demonstrated that laticifers are appealing models with many evolutionary and physiological implications (Hagel et al., 2008; Pickard, 2008; Agrawal and Konno, 2009; Castelblanque et al., 2017). Laticifers also represent attractive natural biofactories with a vast array of potential commercial applications (Hagel et al., 2008; Castelblanque et al., 2017). Understanding the mechanisms of Ni bioaccumulation could therefore increase the likelihood of developing hyperaccumulators as a source of highly enriched Ni fluids (Hagel et al., 2008).

Current understanding indicates that laticifers provide an effective location to synthesize and store a wide array of secondary compounds (Metcalfe, 1967; Hagel et al., 2008). However, our understanding of metal accumulation in laticifers remains limited. This study aimed to

elucidate the distribution and arrangement of Ni-enriched laticifer in the model species *P. acuminata* and bridge the gap between the structure and function of laticifers in metal accumulation. In addition, there is currently no evidence of long-distance transport in laticifers. While transport systems have been intensively studied in the plant kingdom, from transport-specialized cell types (xylem, phloem, aerenchyma) to symplastic transport, the possible long-distance transport in laticifers and their physiology stand as a *terra incognita* (Pickard, 2008). A crucial question therefore emerged: how does Ni transport to the laticifers and does this demonstrate that laticifers are not "only" a storage site? A persistent limitation for investigations aiming to unravel the physiological roles of Ni-laticifers is the visualisation of laticifers *in situ.* Because their contents are under high turgor pressure, even slightly damaged laticifers burst violently expelling their contents (Pickard, 2008; Castelblanque et al., 2017).

Synchrotron X-ray fluorescence microscopy (XRF microscopy) is a powerful technique to quantitatively determine element concentrations in plant material, with use of current instruments commonly attaining a spatial resolution of 0.5–2 µm and sensitivity down to <10 µg g^{-1} for transition elements in areas 10–100 mm^2 (Kopittke et al., 2018; James et al., 2019). X-ray beams, with energies up to 21 keV, and at some facilities up 45 keV, are used to excite X-ray fluorescence of a suite of elements of interest, which are collected by energy-resolving detectors. Other signals induced in this process include X-ray scatter (Compton and Raleigh) and information from absorption of the incident beam. Images indicating elemental distribution are derived from the detected fluorescence signals while images formed from scatter and absorption signals can infer structural information. Measurements can be undertaken in air, at ambient temperature and atmospheric pressure, or under cryogenic conditions (nitrogen cryo-stream or cryogenic chamber) to maintain samples in a frozen-hydrated state. The most common synchrotron XRF experiments acquire elemental maps from the 2 lateral dimensions of flat or thin samples such as leaves or tissue cross-sections, but XRF micro-computed tomography (XRF-µCT) enables reconstruction of 'virtual' lateral slices or volume renders of elemental data from a rotation series of 1 or 2-dimensional projection images (de Jonge & Vogt 2010; van der Ent et al., 2018; Spiers et al. 2022). However, the acquisition of full 3-dimensional XRF-µCT datasets is time-consuming since both lateral and the rotational dimensions must be scanned sequentially. Thus, XRF-µCT is often most efficiently employed to obtain single (or sometimes multiple) virtual tomographic "slices" in physically intact specimens. Synchrotron X-ray phase-contrast imaging microtomography (PCI-µCT) provides

a complementary modality by enabling time-efficient high-resolution volume-based visualisation of the 3D morphology, since the full sample measurement area (the "full-field") is imaged at each rotation angle (Spiers et al. 2022). In contrast to standard X-ray absorption-based imaging, PCI exploits the phase shift of the X-ray beam through the sample (Snigirev et al., 1995) as an additional form of contrast. In many biological specimens which are only weakly absorbing at hard X-ray energies, this can be orders of magnification larger than attenuation (Lewis et al., 2003). The simplest mode of obtaining phase contrast is propagation-based, whereby a small sample-detector distance is introduced. Self-interference of the phase-shifted X-rays yields detectable fringes of intensity corresponding to material interfaces, causing an edge-enhancement effect. Phase retrieval image algorithms can then be used as filters to convert edge-type contrast into a more recognisable area-type contrast with an improved signal-to-noise ratio (Paganin et al. 2002). PCI-μCT has been widely applied to biomedical specimens, but is also useful in the plant sciences (Brodersen et al. 2013; Lauridsen et al. 2014; Charrier et al. 2016).

PCI-μCT provides a reduced total acquisition time in acquiring high-resolution 3D volume data sets in comparison to XRF-μCT, albeit without elemental sensitivity. PCI-μCT requires (partial) absorption of the incident X-ray beam by the sample, but reconstruction of XRF-μCT is actually compromised by absorption of the incident X-ray beam and absorption by the sample of its own fluoresced photons. This effect is commonly jointly referred to as "self-absorption" and it effectively limits the presented sample diameter, while the sample volume analysed in PCI-μCT is predominantly limited by the size of the beam. Thus, overall XRF-μCT and PCI-μCT are highly complementary in gaining insights into the elemental distribution and localization within anatomical structures of plant tissues.

The extraordinarily high Ni concentration of the latex of *P. acuminata* allows for in-depth visualisation of laticifers. Here, we use a novel combination of XRF, XRF-μCT and PCI-μCT 2D and 3D *in situ* elemental and structural data to determine the Ni distribution in the plant shoots (apex, leaves, and petioles) and roots. We thus visualised, for the first time, the distribution, arrangement, and structure of Ni-rich laticifers in three dimensions using an *in-situ* model in leaves, roots, petiole, apical tip and leaf primordia.

Materials and Methods

Collection of plant samples and preparation for the synchrotron analysis

The plant samples of *Pycnandra acuminata* were collected in a rain forest remnant on ultramafic soil at Plaine des Lacs in New Caledonia (22°16'29"S; 166°54'13"E). Two seedlings (30–40 cm tall) were collected with their root systems intact. In addition, whole branches were obtained from the canopy of a mature *P. acuminata* tree with a pole pruner, packed in moist paper, and brought to DESY (Deutsches Elektronen-Synchrotron) in a fresh state. Tissue samples were fixed in 3% glutaraldehyde (in PBS), sectioned with a vibratome (Leica VT1000s), and stained with Toluidine Blue and then imaged with a bright field microscope (Aperio XT Slide Scanner) to aid in the identification of anatomical features.

Synchrotron X-ray fluorescence microscopy, and phase contrast microtomography

The X-ray fluorescence (XRF) microscopy, microtomography (XRF-μCT), and phase contrast imaging microtomography (PCI-μCT) experiments were undertaken at PETRA III (Deutsches Elektronen-Synchrotron, DESY), a 6 GeV synchrotron on the undulator beamline P06 using a cryogenically cooled double-crystal monochromator with Si(111) crystals. The first experiment, comprising XRF 2D elemental mapping and XRF-μCT, was conducted at 14 keV. A KB mirror pair was used to focus the beam to 700 × 530 nm. XRF detection was performed with a Maia 384C detector system in backscatter geometry (Kirkham et al., 2010; Siddons et al., 2014; Ryan et al., 2014). The second experiment included XRF 2D elemental mapping and XRF-μCT alternately with PCI-μCT and was conducted at 12 keV. A stack of 44 Beryllium Compound Refractive Lenses (CRLs) (RXOPTICS, Monschau, Germany) focused the beam to 500 × 500 nm for the XRF components of the experiment. The CRLs were moved laterally out of the beam to enable full-field PCI with a beam size of approximately 1 × 1 mm. The XRF detection scheme was comprised of a 50 mm^2 SII Vortex EM Si-drift detector (Hitachi High-Tech, Chatsworth, California, USA) in 90° geometry. A calibrated PIPS diode (Mirion Technologies (Canberra), Germany) downstream of the sample measured the x-ray transmission concurrently with the XRF scans. For the PCI-μCT, full-field projection images were acquired with a PCO.edge sCMOS detector and scintillator coupled to an Optique Peter microscope tower, in transmission geometry approximately 30 mm directly downstream of the sample. The combination of optical and geometric magnification produced an effective pixel size of 0.47 μm in the detected image.

A number of scan modalities were used, utilising three scanning axes (horizontal (x), vertical (y) and rotation (θ)). For the XRF scans, the horizontal axis was always set as a fast,

continuous-scanning axis to minimise dead-time, with either the vertical axis or the rotation axis used as the slow axis for conventional 2-dimensional XRF elemental mapping and tomography scans (XRF-μCT), respectively. XRF-μCT scans were conducted as either single-slice (x-θ) 2-dimensional scans or as multi-slice data sets, *i.e.,* separate single-slice scans collected at multiple points along the vertical axis, to produce multi-slice tomography sets in the 3 dimensions. The minimum step size used in any of the XRF scans, 0.5 μm, compares to the beam size such that it is feasible to treat the resolution of those resultant images as being equal to the step size. The XRF-μCT scans were comprised of multiple sub-scans of the same spatial region but with complementary sets of angles through 360°, interleaved such that the sets were equally offset from each other. This allows each sub-scan to be aligned individually so as to minimise the effects of vertical drift of the samples over time (scan parameters in Table S1). Full-field PCI-μCT data sets comprised multiple projection images acquired through either 180° or 360° of the rotation axis, with the full details provided for each scan in Table S1.

Samples for each scanning scheme were optimally prepared to preserve internal features. All tomographic scans were performed on fresh pieces cut to at least 2 cm in length to preserve whole laticifers, with the scan areas selected at least 1 cm from a cut end. These samples were frozen *in situ* within 10 minutes after excision, at the beamline sample position under a cryostream operated at -140°C (Oxford Cryosystems 700 Series Cryostream Cooler, Oxford, UK) and remained under the cryostream for the full duration of their measurement; *i.e.,* through all XRF-μCT and PCI-μCT measurements, as relevant. Room temperature scans (~23°C) were performed on fresh planar or hand-sectioned samples. The fresh hydrated samples were hand cut with a stainless-steel razor blade ('dry knife'), mounted between two sheets of Ultralene thin film (4 μm), and adhered to a custom 3D-printed plastic sample frames, to form a tight sandwich and limit evaporation. Hand cut samples were analysed within 10 minutes after cutting. The one freeze-dried sample was prepared by lyophilization at -50°C. The sample frames were placed in the beam focus using magnetic kinematic sample mounts. Scans were performed at high speed to keep the scan time to a minimum. The sample preparation method and the corresponding experimental settings for each image are described in Table S1.

Data processing and statistics

The XRF spectra collected using the Maia detector system were analysed using GeoPIXE (Ryan et al., 1990a; 2005), and images were generated using the Dynamic Analysis method (Ryan and Jamieson, 1993; Ryan, 2000). The XRF spectra collected using the Vortex detectors

were analysed using PyMca (Solé et al. 2007). In addition to elemental concentration mapping, maps of Compton scattering were also derived from spectral scatter peaks, whilst X-ray absorption maps were extracted from the PIPS diode transmission measurements. Analysis of the tomographic data consisted of an alignment step using consistency and cross-correlation methods to correct for horizontal drift in the sinograms followed by a tomographic reconstruction step. Due to a higher angular sampling, reconstruction of the high-resolution sinogram was performed using a filtered-back projection algorithm. The low-resolution sinograms with lower angular sampling were reconstructed with a maximum-likelihood expectation-maximization algorithm based on the functions of the scikit-image library. The 3D visualisation of multi-slice XRF-μCT tomograms was performed using the visualisation software Drishti (Limaye, 2012). For the PCI microtomography data, images were flat-field corrected and then re-aligned via cross-correlation to correct for sample drift. After 2×2 binning the data to increase the signal to noise ratio, tomographic reconstructions were performed using the TomoPy toolbox. A Paganin-type filter was first applied to retrieve the approximate phase data and maximise the area contrast. Then the 3D data was reconstructed with the grid-rec algorithm plus parzen filter. The 3D volume manipulations and renderings of the PCI microtomography data were performed in Avizo (Version 2020, ThermoFisher Scientific). XRF maps, XRF-μCT single slices, and slices of the PCI-μCT data were visualised using the image software Fiji (Schindelin et al. 2012).

Results

Laticifer networks in the whole leaf

The XRF elemental mapping of fresh leaves revealed a Ni-rich laticifer route along the major veins as well as a dense network throughout the leaf mesophyll, where a myriad of laticifers cross over the lamina; Ca deposits are clearly visible along the midrib (Fig. 1b). The high-resolution Ni elemental images of the leaf reveal lateral departure of laticifers, following primary to secondary veins (Fig. 2a-b). The concentration of Ni varies considerably across the lamina (Fig. 2a) and the distribution of laticifers (magenta) is seen to closely follow the venation network (represented by the Compton signal in green) (Fig. 2b). The laticifers are of the articulated type *i.e.,* composed of a series of elongated cells joined together at articulation site (Fig. 2c-e). We note the particularly high Ni concentrations at the swollen laticifer end-walls (bright yellow, Fig. 2c, e, bright cyan, Fig. 2d.). Each laticifer cell examined was typically about 25 μm diameter and 300–1000 μm long and highly enriched in Ni. We observed

anastomosis between cells where laticifers lie side-by-side, allowing Ni passage (Fig. 2e). This anastomosis gives rise to a branching system. Laticifers send out elongated branches into the leaf tissues (Fig. 2e). Nickel concentrations vary along laticifers, partly because of higher concentrations in the end-wall and branch departure, but the elemental map clearly shows a continuous distribution of Ni in the laticifers, likely in a large central vacuole. We also observed the presence of large circular vesicles, devoid of Ni, in many laticifers which we interpret as being lutoids, and the presence of Ca oxalate (Fig. 2d). High concentrations of Ni were also observed in the adaxial epidermis from cross-section of leaves (Suppl Fig. S1).

Laticifer networks in *Pycnandra acuminata* leaf midrib, petiole, and apical tip

Physical cross-sections prepared by hand-cutting a midrib and petiole led to complete destruction of the laticifers cells as can be seen from the 'leaking' and smearing in the Ni XRF elemental maps (Suppl Figs. S1 and S2). Sequential XRF-μCT and PCI-μCT tomography of a second leaf midrib (with blades excised) demonstrate non-destructive and complementary visualisation of intact laticifers (Fig. 3). In a Nickel, Calcium and Absorption composite image, Nickel (cyan) can be seen within a single XRF tomographic slice (Fig. 3a) in the epidermal cells and in laticifers around the phloem and in the cortex. Calcium (red) is observed near the outer surface of the midrib in the epidermal cells. Deeper deposits of Ca cannot be visualised with this method due to absorption of the low-energy Ca signal. The Absorption signal (grey) show voids with empty cells. A volume rendering of the Ni signal from 21 single XRF-μCT tomographic slices reveals laticifer structures including articulations (Fig. 3b). The PCI-μCT reconstructed longitudinal slice of the midrib (Fig. 3c) shows filled (white) and empty (black) laticifers. A cluster of voids are visible to the right, similar to those apparent in Fig. 3a. A pair of Ni-filled (cyan colour) and no-Ni/empty (burgundy colour) laticifers, which can be identified in the horizontal reconstructed slice (Fig. 3d), are visualised in isolation with a 3D volume rendering following partial segmentation of the reconstructed PCI-μCT volume (Fig. 3e). The articulations between the laticifer cells are clearly visible.

An XRF Ni map of part of a foliar petiole (Fig. 4a) reveals many Ni-rich laticifers extending lengthwise along the petiole; depth (lateral) information for the structure of these laticifers is revealed by XRF-μCT (Fig. 4 b-d). A single slice tomogram (Fig. 4b, c) showed large laticifers in the petiole cortex, enrichment of Ni in the epidermis, and Ca-oxalate crystal deposits in the outer cortex (Fig. 4b). The superposition of Ni on the Compton image of the petiole reveals that smaller diameter conduits occur in a location corresponding to the phloem tissues (blue

dots in arc shaped distribution) (Supporting Information Fig. S1), but these conduits are also laticifers. A volume rendering of 39 reconstructed XRF-μCT single slices (Fig. 4d) demonstrates variation in the diameter of the laticifers, distribution of Ca-oxalate in the outer cortex and of Ni in the epidermal cells. The enlargement (Fig. 4e) shows two laticifer cells joining in an articulation. A PCI-μCT volume rendering of a different petiole (Fig. 4f-g) reveals three laticifers distributed at the periphery of the petiole, just under the epidermis. The three laticifers are isolated and volume rendered in fig. 4h, revealing the high Ni concentration and diameter enlargement at articulation site.

Synchrotron XRF mapping of a complete hydrated apical tip reveals a highly dense network of laticifers in the shoot meristem and leaf primordia (Fig. 5a). The cross-section of this apical tip shows an intense Ni concentration in the cortex (Fig. 5b). Comparing the longitudinal views of a single leaf primordia, it is observed that the projection of background Ni content in the 2D XRF map (Fig. 5c) obscures laticifer detail, while in the PCI longitudinal slice (Fig. 5d), single laticifers are clearly distinguishable. In the XRF-μCT single slice of the leaf primordia, the contribution from highly Ni-enriched laticifer network in the cortex obscures the view on individual laticifers cells (Fig. 5e), but these become clearer in the reconstructed PCI volume rendering (Fig. 5g). A composite image of Ni and Compton of a leaf primordial reconstructed from multiple (31) XRF-μCT slices reveals Ni-enriched laticifer in the meristematic tissues (Fig. 5f). The volume rendering of PCI-μCT with background and isolated laticifers (Fig. 5g, h) clearly shows branching of the laticifers as they form in the tip, which will ultimately form into the networks observed in the leaf.

Laticifer networks in *Pycnandra acuminata* root

The XRF-μCT single slice of a root (Fig. 6a) showing Ca and Ni reveals large laticifers cells (50–60 μm diameter) occurring in the cortex and the pith. Reconstructed XRF-μCT absorption visualisation of this slice (Fig. 6b) indicates cells in the pith that appear to be empty. PCI-μCT data of the equivalent XRF-μCT slice provides much better density contrast of the tissue layers and clearly shows the structure of cells and Ni-loaded and empty cells (Fig. 6c). Longitudinal views of a second root (Fig. 6d-h) show the projected Ni elemental map of laticifers (Fig. 6d) and PCI-μCT renderings (Fig. 6e-h), thus revealing successive large laticifer cells that are joined end-to-end. A Ni concentration gradient in these laticifer cells (lower at their tip) is clearly visible, and associated with root elongation. PCI-μCT demonstrates both the isolation of the higher density laticifers (Fig. 6g) and localisation of laticifers within the tissue layers of

the root (Fig. 6 e, f, g), allowing for excellent 3-dimensional visualisation of these complete laticifers through a significant length of the root. A 3D movie reconstruction shows the location of Ni-enriched laticifers in the cortex (Movie 1).

Discussion

Compartmentation of Ni in the plant-level laticifer network

The extremely high Ni concentrations found in *P. acuminata*, the highest concentration ever recorded in a plant (Reeves, 2024), raises the question of how plants can survive with such high metal content in their cells. Hydroponic dosing experiments have further shown that *P. acuminata* is exceptionally tolerant to Ni concentrations in solution (up to 3000 µM) (Isnard et al., 2020). Our *in vivo* visualisation uncovered a previously unknown distribution of articulated laticifers, constituted of a series of cells, united and branched, completely filled with Ni-rich latex, crossing roots, stem, petiole, and leaves. In contrast, we found that Ni concentrations in both xylem and phloem sieve-tube element (leaf and stem) are low. The extremely high level of Ni tolerance in *P. acuminata* is consequently related to the plant scale distribution and large internal volume of laticifer cells, which allow for compartmentation of Ni within the plant. Hyperaccumulation of Ni within the laticifer did not involve modification of the laticifer structure, as the observed laticifer corresponded with the anastomosing articulated type (Rudall, 1987; Evert, 2006; Ramos et al., 2019).

Laticifers involved in Ni transport

In contrast to the knowledge about pressure-driven mass-flow theory involved in phloem translocation and the cohesion-tension hypothesis involved in xylem water movement, there is a paucity of information about the possible long-distance transport within laticifers (Hagel et al., 2008). The current paradigm in metal transport involves xylem loading and long-distance transport (Rascio & Navari-Izzo, 2011), followed by Ni translocation to leaves *via* the phloem (van der Ent et al., 2018). Besides a “classical” Ni pathway involving xylem and phloem, our work suggests another Ni transport pathway within the plant, involving the laticifers that transport Ni from the roots throughout the plant. We posit that the distribution of Ni concentration entails Ni trafficking at articulation sites (end-to-end transport), and symplastic transport through end-wall pitting. Intracellular translocation within laticifers has previously been advocated, but not investigated (Kutchan, 2005). The swollen end-walls (Fig. 2d) showed a stage of perforation, as previously drawn (Evert, 2006), and end-walls became less evident

as laticifers mature. The fact that *P. acuminata* fruits contain high concentrations of Ni (0.3–0.5 Wt%) (Jaffré et al., 1976; Sagner et al., 1998), with the highest amount, 1.4 %Wt, being measured in the rudimentary endocarp (seed) (Sagner et al., 1998), suggests that Ni transport in the laticifer already occurs at the stage of seed germination (Isnard et al., 2020).

A new model for Ni trafficking in laticifers

Articulated laticifers extend during growth by conversion of apical meristematic cells into laticifers and they differentiate acropetally (Evert, 2006). Initially articulated laticifers exhibit nuclei and dense cytoplasm rich in ribosomes, rough endoplasmic reticulum, Golgi bodies, and plastids (Evert, 2006). The chemical speciation of Ni in the latex of *P. acuminata* has been the subject of several studies which unequivocally revealed citrate (Lee et al., 1978; Sagner et al., 1998; Schaumlöffel et al., 2003), as well as a minor fraction of malate and methylated aldaric acid (Callahan et al., 2008) as the Ni binding ligands. Biosynthesis of Ni complex with citrate could originate from the Krebs cycle within the young laticifers or in adjacent phloem cells. In the latter stage of laticifer differentiation, complete autophagy of the tonoplast occurs (Evert, 2006), and the lumen of laticifers becomes filled with Ni-rich latex in a large vacuole. We propose a laticifer-to-laticifer transport model of Ni that would involve transient ligand in laticifers, transmembrane transport and new complexation in situ in young laticifers. Because laticifer cells extend to the roots, Ni can be directly loaded into the laticifers, in the form of the citrate complex (or other metal complexes) *via* the plasma membrane, which remains intact and functional throughout the lifespan of laticifer cells (Evert, 2006).

Our preliminary observation suggests laticifers penetrating into the epidermal cells in leaf cross sections (Fig. S1e), as previously observed in Euphorbiaceae (Rudall, 1987). The laticifer-epidermal cell contact could indicate a direct cellular pathway for Ni deposition into epidermal cells, but such assumption requires further investigations, as the pathway from mesophyll to epidermal cell storage remains an open question (Leitenmaier & Küpper, 2013).

Ligands are transient in hyperaccumulators because the main detoxification in hyperaccumulator plants is by storage, and not by complexation (Leitenmaier, 2013). Further studies are necessary to elucidate the processes involved with ion loading and unloading into the laticifers where Ni complexes accumulate at molar concentrations. Physical properties of Ni, namely the X-ray emission energy, high *Z* contrast, and paramagnetic properties, render the Ni-rich laticifer system ideal for investigation using synchrotron XRF,

(synchrotron/laboratory) XRF-μCT, and Magnetic Resonance Imaging (MRI), respectively to follow Ni movement *in vivo*.

A high turgor pressure in the laticifers is essential for the flow of latex during tapping, and it requires water transfer from the phloem apoplast to the laticifer (Jacob et al., 1998; Evert, 2006). The high turgor pressure alone does not constitute evidence of long-distance transport, and neither does the tapping of latex and rapid "refilling" of laticifer, which depend on influx from the sieves tubes of conducting phloem. Seeing that laticifers extend from root-to-shoot, our study elicits the hypothesis that metal (Ni) distribution could constitute an independent transport system, which would establish a new paradigm in long distance transport within plants. Whether the metal complex is transported by diffusion or if there is a coordinated intracellular movement remains a major question (Kutchan, 2005). Linking research on hyperaccumulation and laticifer functioning might bridge this gap, as ligand-mediated processes involve intra- and intercellular translocation in a highly coordinated fashion in hyperaccumulator plants.

Future research

The phenomenal nickel concentrations in the laticifers of *P. acuminata* effectively serve as a tracer probing the structure and organization of laticifers *in situ*. The implications are not only relevant for hyperaccumulator plants, but also improve the general understanding of laticifers in plants. The complementary nature of the different imaging techniques used in this study is evident. The XRF-μCT method provides the ground truth of the elemental mapping to determine the localization of Ni in laticifer cells, but projection elemental maps of the samples are only reasonably achieved using XRF, as multi-slice XRF-μCT over a few thousand slices is currently prohibitively time-consuming. The PCI-μCT method is an efficient way to achieve high resolution volume reconstruction over extended lengths, which proved particularly useful here to view the organization of laticifer cell networks. However, since PCI-μCT is qualitative and not quantitative or element-specific, it must be in conjunction with XRF maps to provide the 'elemental' reference. Limitations of X-ray fluorescence microtomography include self-absorption of the fluorescent X-rays, which means in practice that samples should be relatively small; this is dependent on the X-ray fluorescence emission energy of the element of interest and the sample matrix, but may be ~1-2 mm diameter for Ni in a typical plant matrix, and for greatest efficiency, ideally approximate a 'round' cross-section. This sample geometry is also ideal for high-resolution PCI-μCT, whilst the full-field technique allows for efficiently

imaging over an extended volume. Seeds, roots, and leaf petioles are hence suitable for this technique, and the exceptionally Ni-enriched laticifers of *P. acuminata* presents an ideal testbed for this approach. Future studies should be targeted to reveal the mechanism of Ni loading into laticifer ducts in the roots of *P. acuminata*, as well as laticifer-to-laticifer transport of Ni.

Acknowledgements

We acknowledge DESY (Hamburg, Germany), a member of the Helmholtz Association HGF, for the provision of experimental facilities. Parts of this research was carried out at PETRA III and we would like to thank Gerald Falkenberg for assistance in using P06, Frank Seiboth (CRLs) Stijn van Malderen (PyMca processing) and Peter Modregger for his assistance with the PCI acquisition. Beamtime was allocated for proposals I-20170741, H-20010008 and I-20190028. This research/project was undertaken with the assistance of the Drishti/Drishti Prayog visualisation software developed by the National Computational Infrastructure's VizLab: nci.org.au/drishti. We thank Vanessa Hequet (IRD, Nouméa) for help in collecting the small plants, and Christine Heinz for her help with anatomical interpretations. The authors thank the Province Sud de Nouvelle-Calédonie for permission to collect plant material (APA-NCPS-2018-11, N°3058-2018). The research leading to this result has been supported by the project CALIPSOplus under the Grant Agreement 730872 from the EU Framework Programme for Research and Innovation HORIZON 2020 and The Pacific Fund. V. Gei was the recipient of an Australia Awards PhD Scholarship from the Australian Federal Government. This work was supported by the French National Research Agency through the national program "Investissements d'avenir" (ANR-10-LABX-21 - RESSOURCES21).

Competing interests

The authors declare no conflicts of interest relevant to the content of this manuscript.

Authors contributions

VG, AvdE, SI, BF and PDE conducted the fieldwork and collected the samples. VG, AvdE, SI, SCI, BF, EMP, GE, KMS, DB and PDE conducted the synchrotron XRF experiment. JG implemented bespoke beamline functionality. KMS and DB performed the XRF data processing and analysis. SCI performed the PCI data processing and visualisation. VG and

AvdE performed the histochemical and anatomical studies. SI and AvdE wrote the first drafts of the manuscript. All authors contributed to writing of the manuscript.

References

Abarca, SLF, Klinkhamer PGL, Choi YH (2019) Plant Latex, from Ecological Interests to Bioactive Chemical Resources ». *Planta Medica* 85(11/12): 856-68. https://doi.org/10.1055/a-0923-8215.

Agrawal AA, Konno K (2009) Latex: a model for understanding mechanisms, ecology, and evolution of plant defense against herbivory. *Annual Review of Ecology, Evolution and Systematics* 40(1): 311–331.

Andresen E, Peiter E, Küpper H (2018) Trace metal metabolism in plants. *Journal of Experimental Botany* 69(5): 909–954.

Brodersen CR, McElrone AJ, Choat B, Lee EF, Shackel KA, Matthews MA (2013) In vivo visualisations of drought-induced embolism spread in *Vitis vinifera*. *Plant Physiology* 161: 1820–1829.

Callahan DL, Roessner U, Dumontet V, Perrier N, Wedd AG, O'Hair RA, Baker AJ, Kolev SD (2008) LC-MS and GC-MS metabolite profiling of nickel(II) complexes in the latex of the nickel-hyperaccumulating tree *Sebertia acuminata* and identification of methylated aldaric acid as a new nickel(II) ligand. *Phytochemistry* 69(1): 240–251.

Castelblanque L, Balaguer B, Marti C, Rodriguez JJ, Orozco M, Vera P (2016) Novel insights into the organization of laticifer cells: a cell comprising a unified whole system. *Plant Physiology* 172(2):1032-1044.
Castelblanque L, Balaguer B, Marti C, Rodriguez JJ, Orozco M, Vera P (2017) Multiple facets of laticifer cells. *Plant Signaling & Behavior* 12(7): e1300743.

Charrier G, Torres-Ruiz JM, Badel E, Burlett R, Choat B, Cochard H, Delmas CEL, Domec J-C, Jansen S, King A, Lenoir N, Martin-StPaul N, Gambetta GA, Delzon S (2016) Evidence for Hydraulic Vulnerability Segmentation and Lack of Xylem Refilling under Tension. *Plant Physiology* 172 (3): 1657–1668.

de Jonge MD, S. Vogt S (2010) Hard X-Ray Fluorescence Tomography-an Emerging Tool for Structural Visualisation. *Current Opinion in Structural Biology* 20(5): 606–614.

Evert RF (2006) Esau's Plant Anatomy. Hoboken, New Jersey, USA: A John Wiley & Sons, Inc.

Farrell BD, Dussourd, .E, Mitte, C (1991) Escalation of Plant Defense: Do Latex and Resin Canals Spur Plant Diversification? *The American Naturalist* (138): 881–900.

Gei V, Echevarria G, Erskine PD, Isnard S, Fogliani B, Montargès-Pelletier E, Jaffré T, Spiers KM, Garrevoet J, van der Ent A (2020) Soil chemistry, elemental profiles and elemental distribution in nickel hyperaccumulator species from New Caledonia. *Plant and Soil* 457: 293–320. https://doi.org/10.1007/s11104-020-04714-x

Hagel JM, Yeung EC, Facchini PJ (2008) Got milk? The secret life of laticifers. *Trends in Plant Science* 13(12): 631–639.

Isnard S, L'Huillier L, Paul ALD, Munzinger J, Fogliani B, Echevarria G, Erskine PD, Gei V, Jaffre T, van der Ent A. (2020) Novel Insights Into the Hyperaccumulation Syndrome in Pycnandra (Sapotaceae). *Frontiers in Plant Science* 11:559059.

James S, van der Ent A, Harris HH (2019) Tracking Metal Ions in Biology using X-ray Methods. *Encyclopedia of Inorganic and Bioinorganic Chemistry* doi: 10.1002/9781119951438.eibc2692

Jacob JL, Prévôt JC, Lacote R, Gohet E, Clément A, Gallois R, Joët T, Pujade-Renaud V, D'Auzac J (1998) Les mécanismes biologiques de la production de caoutchouc par *Hevea brasiliensis*. *Plantations, Recherche, Développement* 5: 5–17.

Jaffré T, Brook RR, Lee J, Reeves RG (1976) *Sebertia acuminata*: A hyperaccumulator of nickel from New Caledonia. *Science* 193(4253): 579–580.

Jaffré T, Reeves RD, Baker AJM, Schat H, van der Ent A (2018) The discovery of nickel hyperaccumulation in the New Caledonian tree *Pycnandra acuminata* 40 years on: an introduction to a Virtual Issue. *New Phytologist* 218(2): 397-400.

Johnson AR, Moghe GD, Frank MH (2021) Growing a glue factory: Open questions in laticifer development. *Current Opinion in Plant Biology* 64:102096.

Kopittke PM, Punshon T, Paterson DJ, Tappero RV, Wang P, Blamey FPC, van der Ent A, Lombi E (2018) Synchrotron-based X-Ray fluorescence microscopy as a technique for imaging of elements in plants. Plant Physiology, 178: 507-523.

Kirkham R, Dunn PA, Kuczewski AJ, Siddons DP, Dodanwela R, Moorhead GF, Ryan CG, De Geronimo G, Beuttenmuller R, Pinelli D, et al. (2010) The Maia Spectroscopy Detector System: Engineering for Integrated Pulse Capture, Low‐Latency Scanning and Real‐Time Processing. AIP Conference Proceedings 1234(1): 240-243.

Küpper H, Lombi E, Zhao FJ, Wieshammer G, McGrath SP (2001) Cellular compartmentation of nickel in the hyperaccumulators *Alyssum lesbiacum, Alyssum bertolonii* and *Thlaspi goesingense*. *Journal of Experimental Botany* 52(365): 2291–2300.

Kutchan TM (2005) A role for intra- and intercellular translocation in natural product biosynthesis. *Current Opinion in Plant Biology* 8(3): 292–300.

Lauridsen T, Glavina K, Colmer TD, Winkel A, Irvine S, Lefmann K, Feidenhans'l R, Pedersen O. (2014) Visualisation by high resolution synchrotron X-ray phase contrast micro-tomography of gas films on submerged superhydrophobic leaves. *Journal of Structural Biology188*(1): 61–70.

Lee EJ, Hagel JM, Facchini PJ (2013) Role of the phloem in the biochemistry and ecophysiology of benzylisoquinoline alkaloid metabolism. *Frontiers in Plant Science* 4: 182.

Lee J, Reeves G, Brooks RR, Jaffré T (1978) Relation between nickel and citric-acid in some nickel-accumulating plants. *Phytochemistry* 17: 1033–1035.

Leitenmaier B, Küpper H (2013) Compartmentation and complexation of metals in hyperaccumulator plants. *Frontiers in Plant Science* 4: 374.

Lewis RA, Hall CJ, Hufton AP, Evans S, Menk RH, Arfelli F, Rigon L, Tromba G, D Dance DR, Ellis IO, Evans A, Jacobs E, Pinder SE, Rogers KD (2003) X-ray refraction effects: application to the imaging of biological tissues. *The British Journal of Radiology* 76(905): 301-308.

Limaye A (2012) Drishti: a volume exploration and presentation tool. Proc. SPIE 8506, Developments in X-Ray Tomography VIII, 85060X.

Mahlberg PG (1993) Laticifers: An historical perspective. *The Botanical Review* 59(1): 1–23.

Metcalfe CR (1967) Distribution of latex in the plant kingdom. *Economic Botany* 21(2): 115–127.

Moir GFJ (1959) Ultracentrifugation and Staining of Hevea Latex. *Nature* 184(4699): 1626–1628.

Nawrot R (2020) Latex, Laticifers and Their Molecular Components From Functions to Possible Applications, in: Advances in Botanical Research. Elsevier, pp. 1–238.

Paganin D, Mayo SC, Gureyev TE, Miller PR, and Wilkins SW (2002) Simultaneous phase and amplitude extraction from a single defocused image of a homogeneous object. Journal of Microscopy, 206(1):33–40.

Perrier N, Colin F, Jaffré T, Ambrosi J-P, Rose J, Bottero J-Y (2004) Nickel speciation in *Sebertia acuminata*, a plant growing on a lateritic soil of New Caledonia. *Comptes rendus: Geoscience* 336(6): 567–577.

Pickard WF (2008) Laticifers and secretory ducts: two other tube systems in plants. *New Phytologist* 177(4): 877–888.

Ramos MV, Demarco D, da Costa Souza IC, de Freitas CDT (2019) Laticifers, latex, and their role in plant defense. *Trends in Plant* Science 24(6):553-567.

Rascio N, Navari-Izzo F (2011) Heavy metal hyperaccumulating plants: how and why do they do it? and what makes them so interesting? *Plant Science* 180(2): 169–181.
Rudall P (1987) Laticifers in Euphorbiaceae–a conspectus. *Botanical Journal of the Linnean Society* 94(1-2): 143–163.

Reeves, R.D. (2024) The discovery and global distribution of hyperaccumulator plants: A personal account. *Ecological Research.* https://doi.org/10.1111/1440-1703.12444

Ryan CG, Siddons DP, Kirkham R, Li ZY, de Jonge MD, Paterson DJ, Kuczewski A, Howard DL, Dunn PA, Falkenberg G, et al. (2014) Maia X-ray fluorescence imaging: Capturing detail in complex natural samples. *Journal of Physics: Conference Series* 499: 012002–12.

Ryan CG, Jamieson DN (1993) Dynamic analysis: on-line quantitative PIXE microanalysis and its use in overlap-resolved elemental mapping. *Nuclear Instruments and Methods in Physics Research Section B: Beam Interactions with Materials and Atoms* 77: 203–214.

Ryan CG (2000) Quantitative trace element imaging using PIXE and the nuclear microprobe. *International Journal of Imaging Systems and Technology* 11: 219–230.

Sagner S, Kneer R, Wanner G, Cosson JP, Deus-Neumann B, Zenk MH (1998) Hyperaccumulation, complexation and distribution of nickel in *Sebertia acuminata*. *Phytochemistry* 47(3): 339–347.

Schaumlöffel D, Ouerdane L, Bouyssiere B, Łobiński R (2003) Speciation analysis of nickel in the latex of a hyperaccumulating tree *Sebertia acuminata* by HPLC and CZE with ICP MS and electrospray MS-MS detection. *Journal of Analytical Atomic Spectrometry* 18(2): 120–127.

Schindelin J., Arganda-Carreras, I., Frise, E., Kaynig, V., Longair, M., Pietzsch, T., et al. (2012). Fiji: an open-source platform for biological-image analysis. Nature Methods 9(7), 676–682.

Snigirev A, Snigireva I, Kohn V, Kuznetsov S, Schelokov I (1995) On the possibilities of x-ray phase contrast microimaging by coherent high-energy synchrotron radiation. *Review of Scientific Instruments* 66 (12): 5486-5492. https://doi.org/10.1063/1.1146073

Solé VA, Papillon E, Cotte M, Walter Ph, Susini J (2007) A multiplatform code for the analysis of energy-dispersive X-ray fluorescence spectra. *Spectrochimica Acta Part B* 62: 63–68.

Spiers KM, Brueckner D, Garrevoet J, Falkenberg G, van der Ent A (2022) Synchrotron XFM tomography for elucidating metals and metalloids in hyperaccumulator plants. *Metallomics* 14(11):mfac069. doi: 10.1093/mtomcs/mfac069.

van der Ent A, Przybyłowicz WJ, Jonge MD, Harris HH, Ryan CG, Tylko G, Paterson DJ, Barnabas AD, Kopittke PM, Mesjasz-Przybyłowicz J (2018) X-ray elemental mapping techniques for elucidating the ecophysiology of hyperaccumulator plants. *New Phytologist* 218(2): 432–452.

Ziegler J, Facchini PJ (2008) Alkaloid biosynthesis: metabolism and trafficking. *Annual Review of Plant Biology* 59: 735–769.

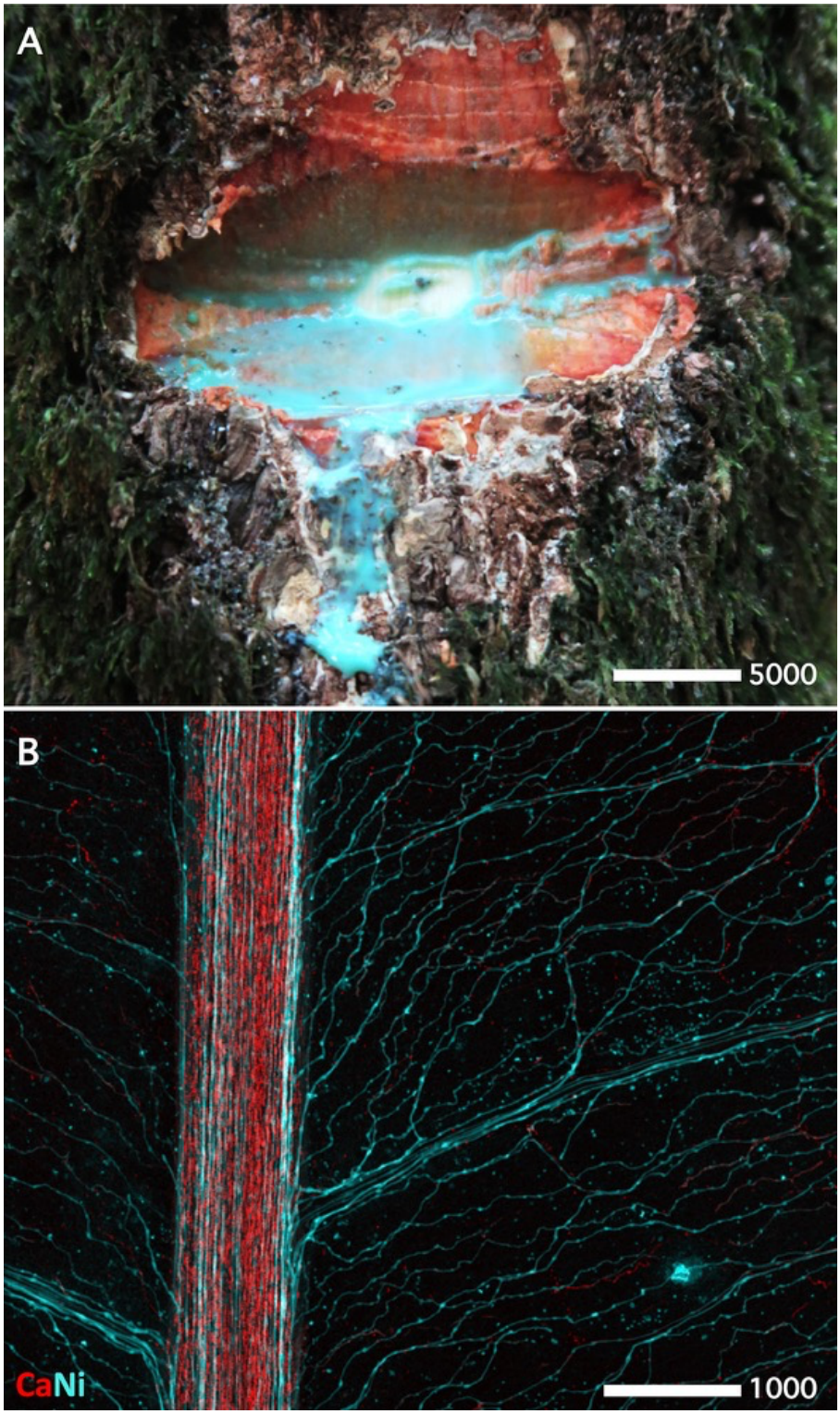

Figure 1. Exuding latex and Ni-rich laticifers in hydrated *Pycnandra acuminata* leaf. (a) The blue Ni-rich latex exudes readily from damaged bark of the main trunk; (b) Synchrotron XRF elemental map of the laticifer network following major veins (Ca: red, Ni: cyan). The highest density of laticifers is along the primary and secondary veins, but they branch abundantly

throughout the mesophyll and a myriad of laticifers cross over the lamina. Scale bars denote 5000 and 1000 μm.

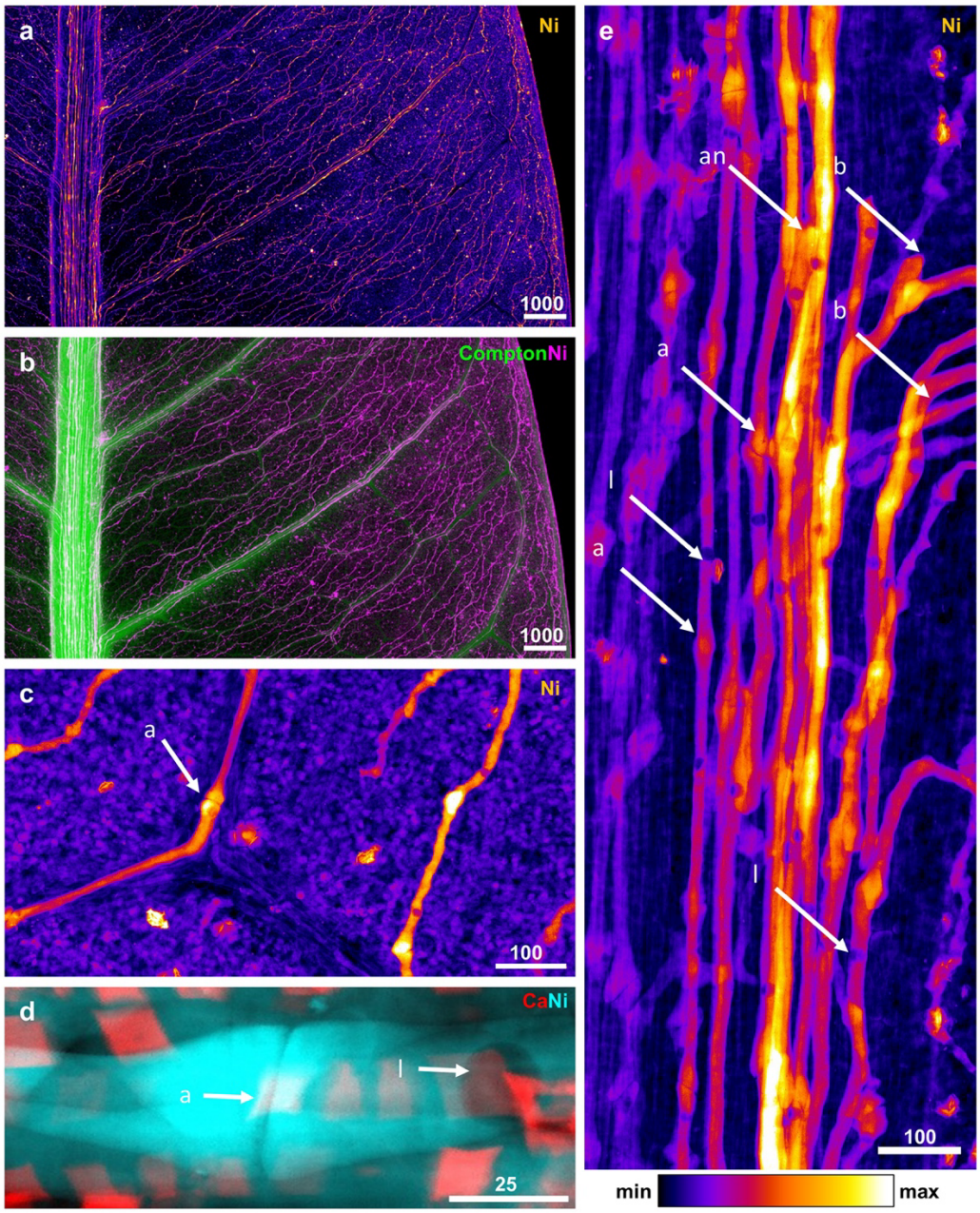

Figure 2. Synchrotron XRF maps of nickel-rich laticifers observed from paradermal scans of a fresh leaf of *Pycnandra acuminata*. (a, b) Ni-rich laticifer network following major veins. Laticifers follow the midrib, and departure of several laticifers along secondary veins and throughout the mesophyll are observed (Ni: magenta, Compton (representing veins, structures): green). (c-e) High-resolution scans of a smaller area of leaf exposes more details on the structure of the laticifers. (c) Laticifers are connected *via* their end-wall (articulation), forming long tubes whose latex is highly enriched in Ni. Ni-concentration is higher at end-walls connecting laticifers. (d) Detail of laticifer articulation (Ca: red, Ni: cyan). (e) Laterally,

the laticifers are connected *via* anastomosis. Abbreviations: a, articulation; an, anastomose; b, branching laticifer; l, lutoid. Scale bars denote 25, 100 and 1000 μm.

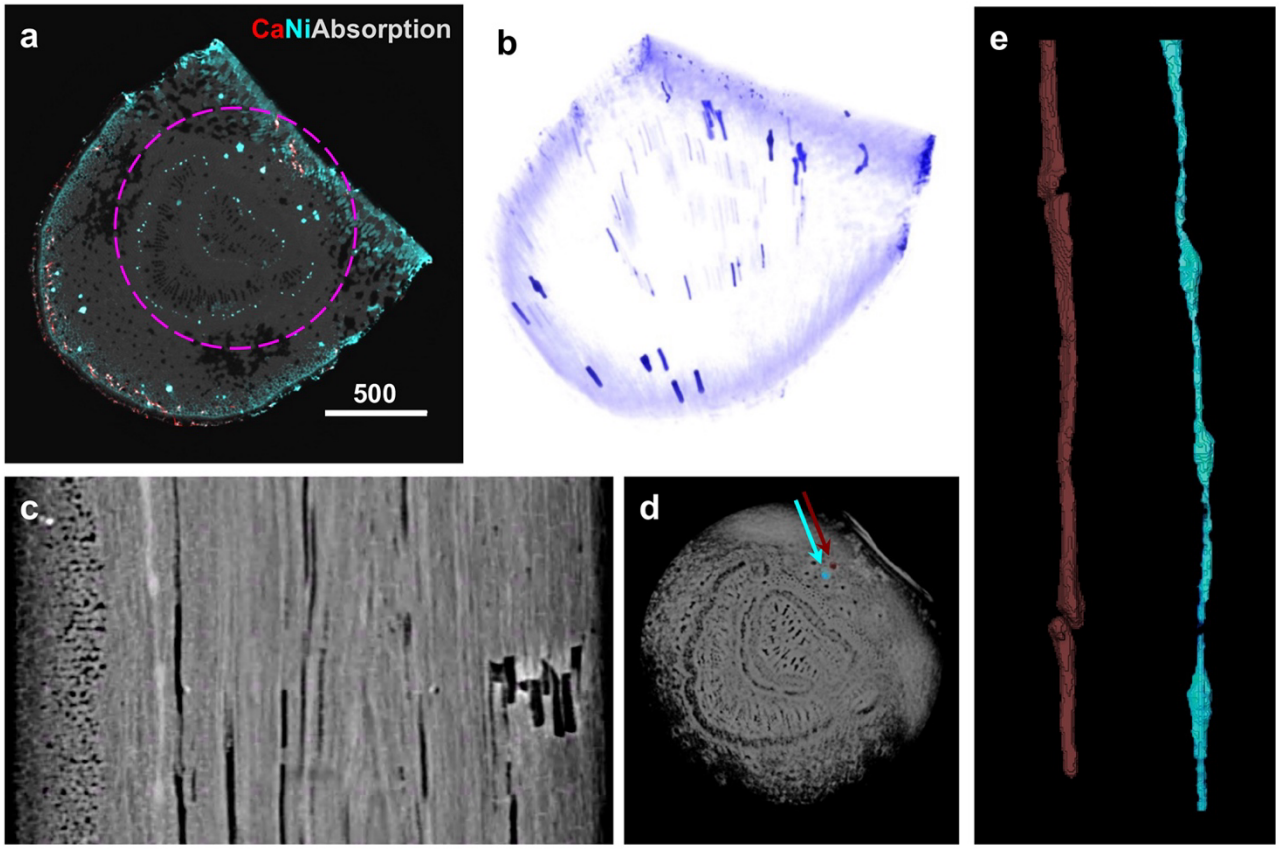

Figure 3. Synchrotron XRF-µCT and PCI-µCT reconstructed images observed from a fresh leaf midrib of *Pycnandra acuminata*. (a) XRF-µCT single slice reconstruction (Ca: red, Ni: cyan) superimposed over absorption signal (grey). (b) 3D volume rendering of the XRF-µCT reconstruction of this petiole (Ni: blue). (c,d) PCI-µCT reconstruction with longitudinal and horizontal slices of the midrib respectively. (e) Isolated volume rendering of two laticifers cells (empty cells: burgundy, Ni-loaded: cyan) following partial segmentation of the reconstructed PCI-µCT volume. Arrows indicate the positions of these two isolated laticifer cells in panel d. Scale bars denote 500 µm.

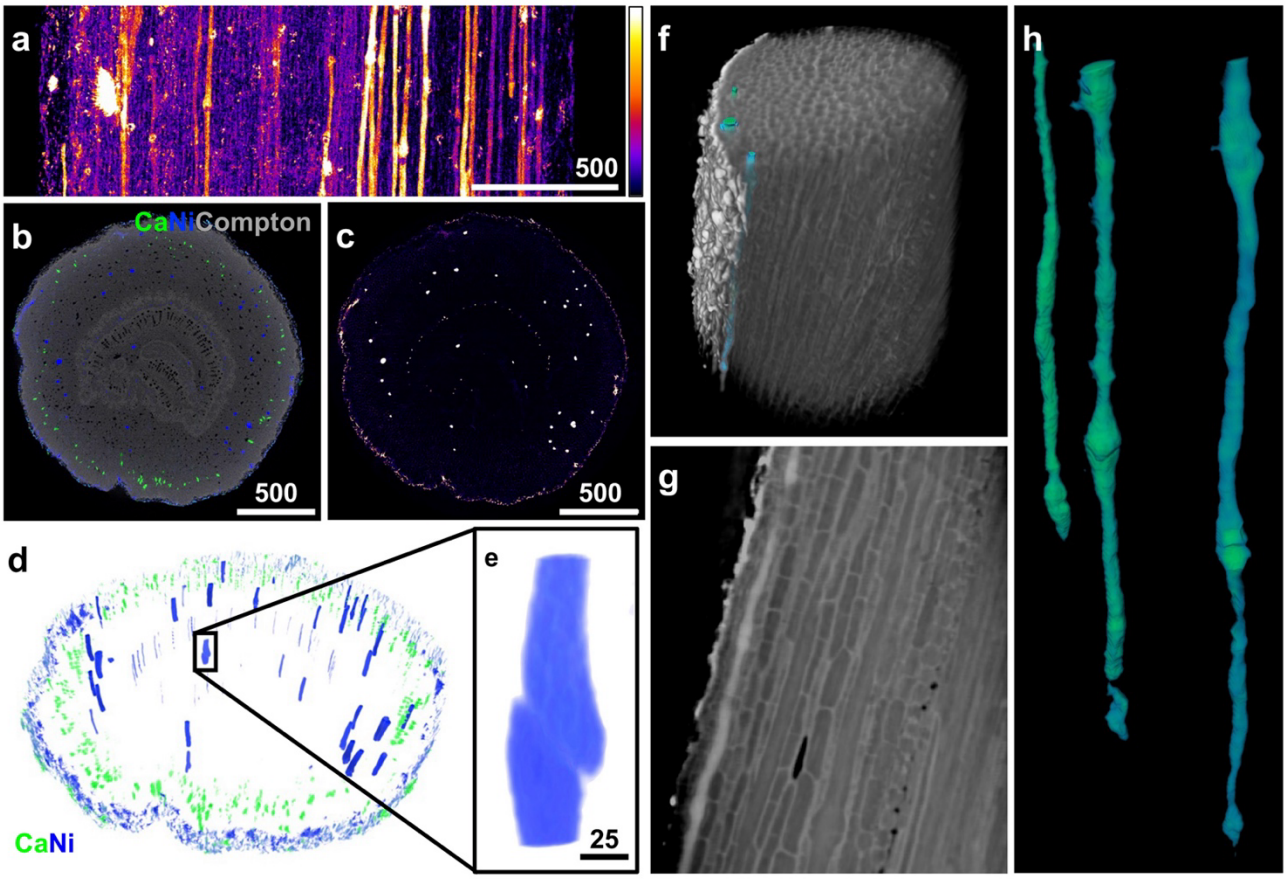

Figure 4. Synchrotron XRF elemental mapping, XRF-µCT and PCI-µCT reconstruction of a foliar petiole. (a) XRF elemental map of Ni showing highly Ni-enriched laticifers. (b) Composite of Compton, Ca and Ni XRF-µCT images. The Compton map provided information on the internal composition and revealed the distribution of the laticifers in the petioles. Numerous laticifers are distributed throughout the cortex (dark structures); a few still contained Ni (blue dots), and smaller dots form an arc shape at the periphery of wood, with laticifer distributed within in the phloem tissues. (c) the relative concentration of Ni in this XRF-µCT slice. (d) 3D volume rendering of multiple reconstructed XRF-µCT slices. The enlargement (e) shows two single laticifer cells joining in an articulation (Ca: green, Ni: blue). (f-h) PCI-µCT visualisations of another petiole; (f, h) Three Ni-filled laticifers are volume rendered in blue-green (with green indicating higher Ni concentration) in context with the grey petiole tissue volume (f) and in isolation (h). (g) The bright contrast of a laticifer in the outer cortex (pale grey) relative to other tissue is demonstrated in the longitudinal reconstructed slice. Scale bars denote 25, and 500 µm.

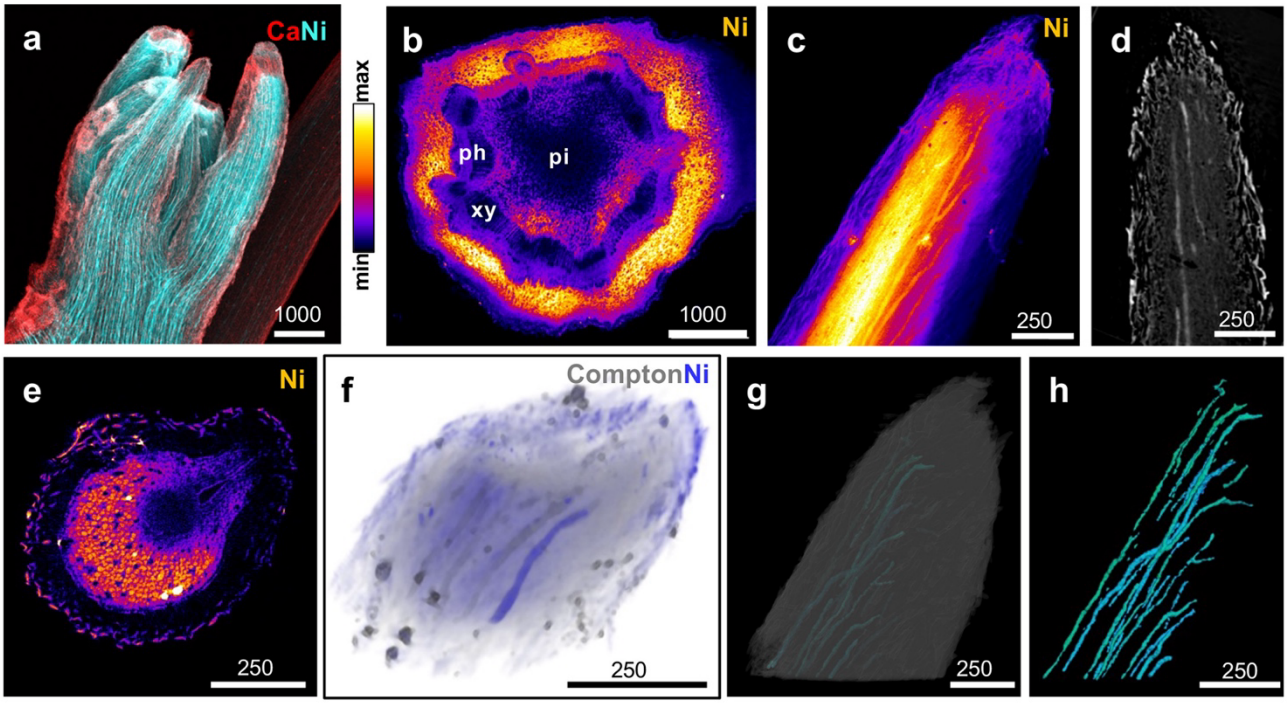

Figure 5. Synchrotron XRF, XRF-µCT and PCI-µCT images of an apical tip and leaf primordia. (a) Synchrotron XRF composite image of a fresh and whole apical tip showing highly enriched Ni-laticifers densely packed (Ca: red Ni: cyan). (b) 2D XRF map of a physically sectioned portion of a hydrated stem under the apical tip, revealing strong Ni-enrichment in the cortex, but no visible individual laticifers. (c) 2D XRF projection map of Ni of a leaf primordium. (d) PCI-µCT longitudinal slice of this leaf primordia. (e) XRF-µCT single cross-sectional slice of a leaf primordia showing Ni. (f) XRF-µCT multiple slice volume rendering of a leaf primordia with Ni (blue) projected over Compton scatter image. (g,h) PCI-µCT volume rendering of a leaf primordia visualising the Ni-loaded laticifers in blue-green, shown in context of the grey root tissue volume (g), and then in isolation (h). Abbreviations: pi: pith; ph, phloem; xy, xylem. Scale bars denote 250 and 1000 µm.

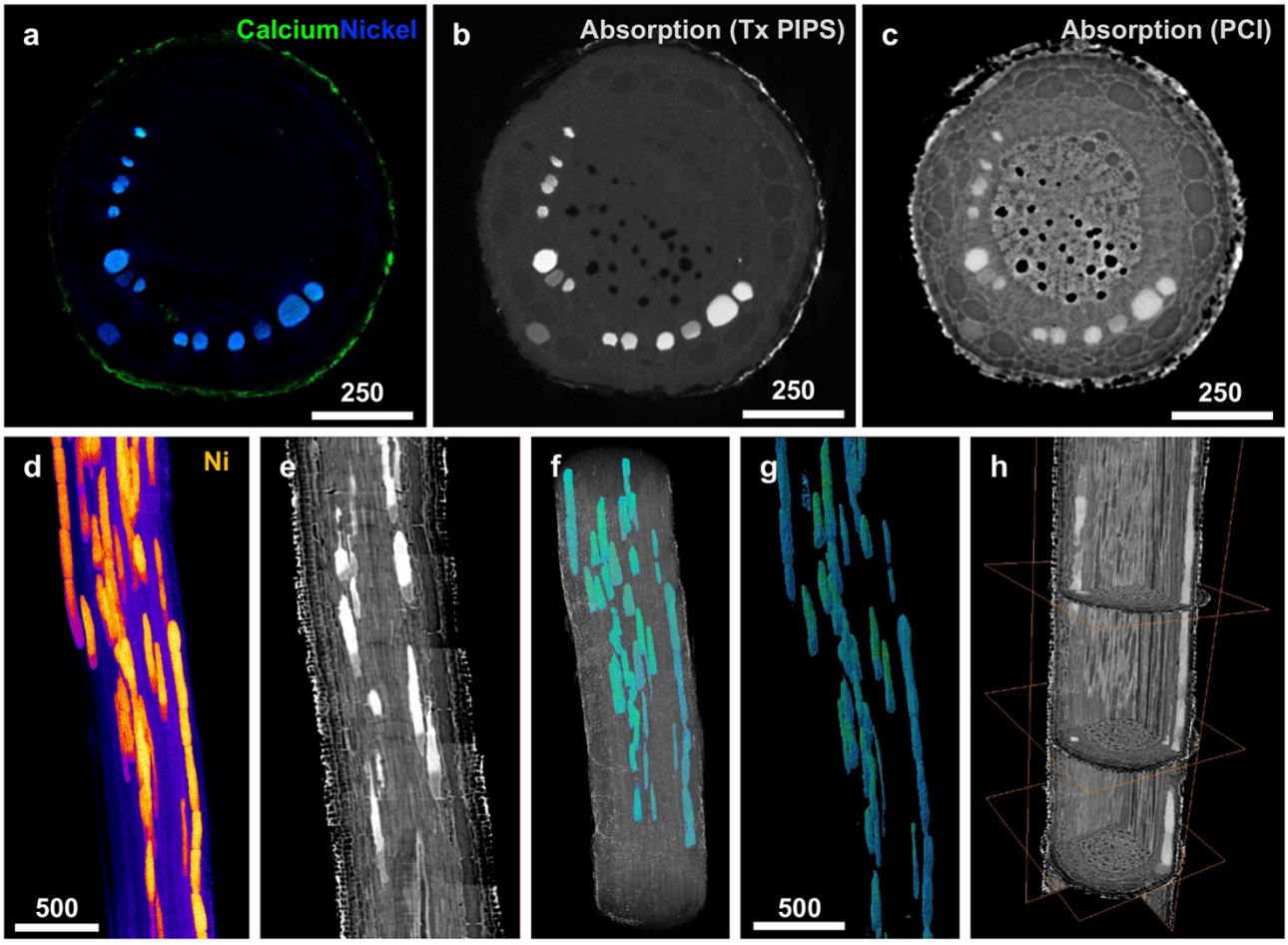

Figure 6. Synchrotron XRF, XRF-µCT and PCI-µCT images of *Pycnandra accuminata* root: (a&b) XRF-µCT single slice (Ni: blue, Ca: green), and the corresponding XRF-µCT absorption measurement. (c) PCI-µCT horizontal slice at the same position as the XRF measurement in a&b. (d) XRF Ni projection of a second root and (e-h) complementary 3-dimensional PCI-µCT visualisations: (e) A greyscale longitudinal reconstructed slice showing lower concentration at the lower end (towards the root tip) in many of the laticifers. (f,g) 3D volume renderings of the partially-segmented laticifer network via thresholding of the higher density values: correlated to medium (blue) and highest (green) Ni concentration, within and isolated from the root tissue respectively. (h) Orthogonal views of the reconstructed data contrasting the longitudinal and lateral structure, including the proximity of some laticifers in the cortex of the root. Scale bars denote 250 and 500 µm.

Supporting Information

In vivo imaging nickel-rich laticifers: a breakthrough in metal hyperaccumulation

Antony van der Ent[1,2,3], Tanguy Jaffré[4,5], Kathryn M. Spiers[6], Dennis Brueckner[6], Sarah C. Irvine[7]Peter D. Erskine[3], Vidiro Gei[3], Emmanuelle Montargès-Pelletier[8], Bruno Fogliani[9], Guillaume Echevarria[2], Sandrine Isnard[4,5]*

[1]Laboratory of Genetics, Wageningen University and Research, The Netherlands.

[2]Laboratoire Sols et Environnement, INRAE, Université de Lorraine, France.

[3]Centre for Mined Land Rehabilitation, Sustainable Minerals Institute, The University of Queensland, Australia.

[4]AMAP, Université de Montpellier, IRD, CIRAD, CNRS, INRAE, Montpellier, France.

[5]AMAP, IRD, Herbier de Nouvelle-Calédonie, Nouméa, New Caledonia.

[6]Deutsches Elektronen-Synchrotron DESY, Germany.

[7]*Institute of Materials Physics,* Helmholtz-Zentrum Hereon, Germany.

[8] Université de Lorraine, CNRS, LIEC, F-54000, Nancy, France.

[9]Institut Agronomique néo-Calédonien (IAC), Equipe ARBOREAL (AgricultuRe BiOdiveRsité Et vAlorisation), New Caledonia.

*Corresponding author: antony.vanderent@wur.nl

Table S1. Sample preparation and scan information for figures utilizing X-ray techniques. Fields not relevant to a scan are left blank.

Figure number	Sample morphology	Sample state	Temp	X-ray Contrast	Detector	Scan mode[1]	Exposure time (ms)	x step size (µm)	y step size (µm)	θ number of angles / total angle traversed	number of interlaced sub-scans[2]	number of slices	step size between slices (µm)	number of stacked scans
1b	Planar	Fresh	RT	XRF	Maia	2D x-y	10	5	5					
2a, 2b	Planar	Fresh	RT	XRF	Maia	2D x-y	8	10	10					
2c	Planar	Fresh	RT	XRF	Maia	2D x-y	0.8	0.6	0.6					
2d	Planar	Fresh	RT	XRF	Maia	2D x-y	0.5	0.3	0.3					
2e	Planar	Fresh	RT	XRF	Maia	2D x-y	0.8	0.6	0.6					
3a	Long piece	Frozen hydrated	Cryo	XRF	Vortex	2D x-θ	5	1		904 / 360	4			
3b	Long piece	Frozen hydrated	Cryo	XRF	Vortex	2D x-θ + y	5	4		452 / 360	2	21	10	
3c, d, e	Long piece	Frozen hydrated	Cryo	FF PCI	PCO	3D FF	500			3600 / 360				
4a	Long piece	Frozen hydrated	Cryo	XRF	Maia	2D x-y	0.5	2	2					
4b, c	Long piece	Frozen hydrated	Cryo	XRF	Maia	2D x-θ	5	0.5		1808 / 360	8			
4d, e	Long piece	Frozen hydrated	Cryo	XRF	Maia	2D x-θ + y	7.5	2		452 / 360	2	39	4	
4f, g, h	Long piece	Frozen hydrated	Cryo	FF PCI	PCO	3D FF	300			1800 / 180				
5a	Long piece	Fresh	RT	XRF	Maia	2D x-y	8	12	12					
5b	Physical section	Fresh	RT	XRF	Maia	2D x-y	6	10	10					
5c	Long piece	Frozen hydrated	Cryo	XRF	Maia	2D x-y	2	2	2					
5d, g, h	Long piece	Frozen hydrated	Cryo	FF PCI	PCO	3D FF	600			3600 / 360				
5e	Long piece	Frozen hydrated	Cryo	XRF	Vortex	2D x-θ	5	1		900 / 360	4			
5f	Long piece	Frozen hydrated	Cryo	XRF	Vortex	2D x-θ + y	5	4		362 / 360	2	31	10	
6a, b	Long piece	Frozen hydrated	Cryo	XRF	Vortex	2D x-θ	10	1		724 / 360	4			
6c	Long piece	Frozen hydrated	Cryo	FF PCI	PCO	3D FF	600			1800 / 180				
6d	Long piece	Frozen hydrated	Cryo	XRF	Vortex	2D x-y	2	2	2					
6e, f, g, h	Long piece	Frozen hydrated	Cryo	FF PCI	PCO	3D FF	300			1800 / 180				5
S1a, S1c	Physical section	Fresh	RT	XRF	Maia	2D x-y	8	6	6					
S1d	Physical section	Freeze dried	RT	XRF	Maia	2D x-y	10	5	5					
S1f	Physical section	Fresh	RT	XRF	Maia	2D x-y	10	7	7					

[1] the three axes are denoted x (horizontal), y (vertical and θ (rotation), 2D x-θ + y: indicates multiple single slice (2D x-θ) scans; the sample is stepped vertically in between each scan. The vertical step distance is indicated as step size between slices

[2] interlaced sub-scans, each comprising the full rotation range and offset from each other for angular distribution, better ensure full angular coverage in the case of data loss during the scan.

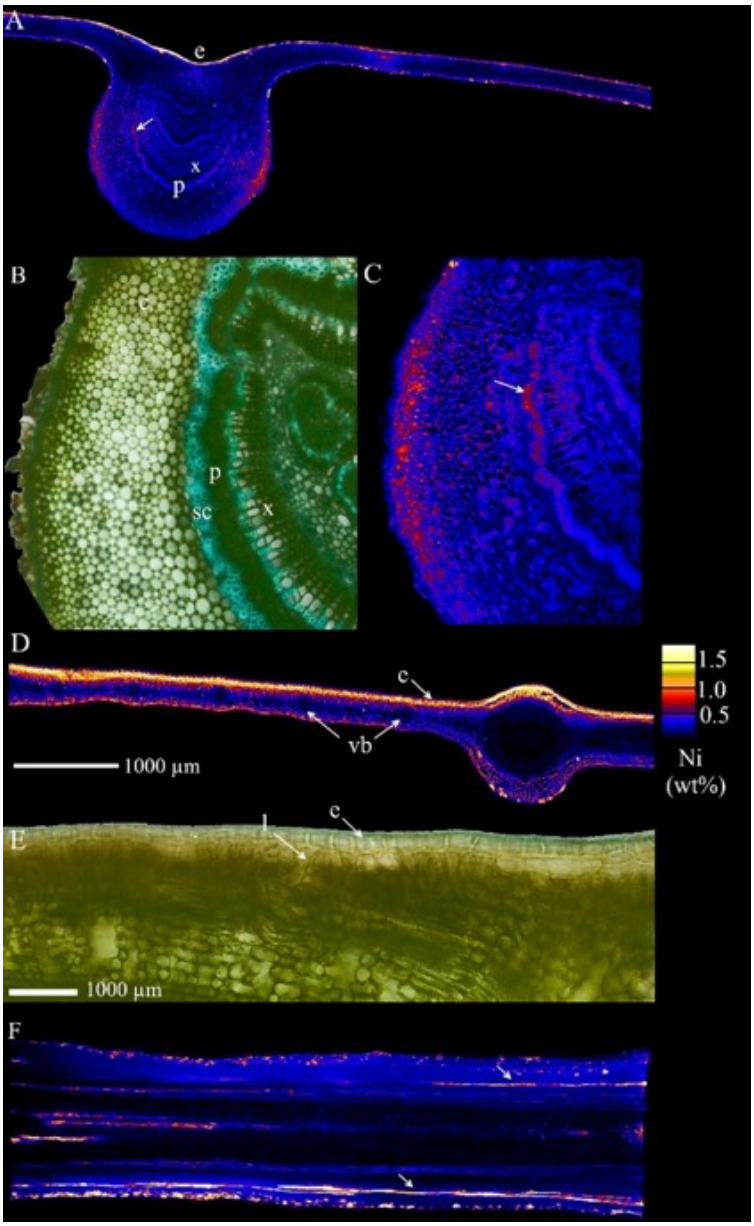

Fig. S1. Synchrotron µXRF maps of Ni from cross-section of leaves of *Pycnandra acuminata*. (A) Ni-map of a fresh cross-section of mid-rib. The highest concentrations were observed strongly localized in the adaxial epidermis. Only few hotspots of Ni are observed in the collenchyma and the mesophyll. (B) Light microscopy image of a toluidine-stained cross-section of the midrib. (C) Close-up view of the mid-rib cross-section showing Ni-spots in a location corresponding to the collenchyma, phloem, and more sparsely in the xylem. Nickel distribution was disrupted and laticifers visible from only few locations as leaf sectioning led to emptying the laticifer, the cell appearing devoid of Ni-rich latex. (D) The distribution of Ni-rich tissues was best preserved in freeze-dried leaf cross-section. The highest concentrations were observed strongly localized in the adaxial epidermis. Ni was not detected in vascular bundles. (E) Longitudinal section of a fresh petiole showing long laticifers. Ni-deposits also occur in epidermal cells of the petiole. l: laticifer; e: epidermis.

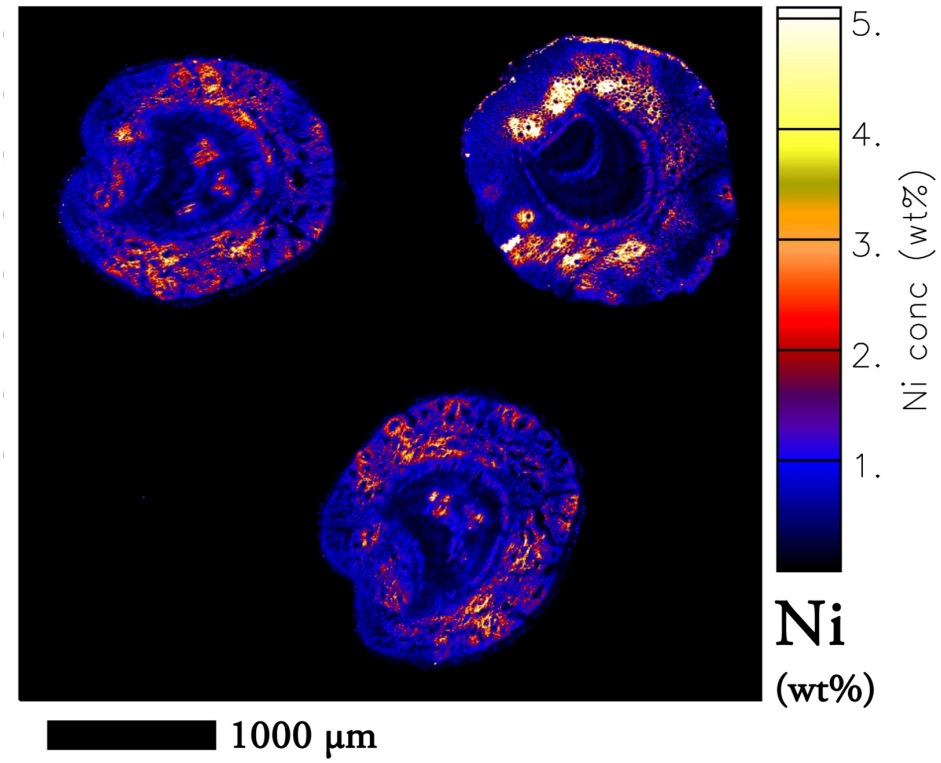

Fig. S2. Synchrotron µXRF maps of Ni from hand cut physical cross-section of fresh/hydrated petioles of *Pycnandra acuminata*. The image clearly shows massive Ni leakage from destroyed laticifers cells.